



CrossMark  
click for updates

Cite this: DOI: 10.1039/c5lc01460c

## IR-Live: fabrication of a low-cost plastic microfluidic device for infrared spectromicroscopy of living cells†

G. Birarda,<sup>ab</sup> A. Ravasio,<sup>c</sup> M. Suryana,<sup>c</sup> S. Maniam,<sup>c</sup> H.-Y. N. Holman<sup>a</sup> and G. Greci<sup>\*c</sup>

Water is a strong mid-infrared absorber, which has hindered the full exploitation of label-free and non-invasive infrared (IR) spectromicroscopy techniques for the study of living biological samples. To overcome this barrier, many researchers have built sophisticated fluidic chambers or microfluidic chips wherein the depth of the liquid medium in the sample compartment is limited to 10  $\mu\text{m}$  or less. Here we report an innovative and simple way to fabricate plastic devices with infrared transparent view-ports enabling infrared spectromicroscopy of living biological samples; therefore the device is named “IR-Live”. Advantages of this approach include lower production costs, a minimal need to access a micro-fabrication facility, and unlimited mass or waste exchange for the living samples surrounding the view-port area. We demonstrate that the low-cost IR-Live in combination with microfluidic perfusion techniques enables long term (>60 h) cell culture, which broadens the capability of IR spectromicroscopy for studying living biological samples. To illustrate this, we first applied the device to study protein and lipid polarity in migrating REF52 fibroblasts by collecting 2-dimensional spectral chemical maps at a micrometer spatial resolution. Then, we demonstrated the suitability of our approach to study dynamic cellular events by collecting a time series of spectral maps of U937 monocytes during the early stage of cell attachment to a bio-compatible surface.

Received 1st December 2015,  
Accepted 14th March 2016

DOI: 10.1039/c5lc01460c

www.rsc.org/loc

## Introduction

A major breakthrough in life science research during the past several decades is live cell imaging. Time-lapse microscopy,<sup>1</sup> light microscopy,<sup>2</sup> and, in particular, fluorescence microscopy have advanced to allow imaging beyond the diffraction limit thanks to the development of techniques like structured illumination microscopy (SIM), stimulated emission depletion (STED) microscopy, photo-activated localization microscopy (PALM) or stochastic optical reconstruction microscopy (STORM).<sup>3–7</sup> Belonging to the family of chemical microscopy techniques, infrared spectromicroscopy (FTIR) uses visible light to identify the morphology of the cells or tissues and the infrared (IR) light illumination and interferometer to produce correlated chemical maps. Illumination with infrared light promotes energy exchanges between the inherent vibrational modes of molecular bonds and incident photons. These exchanges result in distinct, fingerprint-like spectral bands that appear in absorption measured as a function of the wave-

length of incident light (typically expressed in units of wavenumber,  $\text{cm}^{-1}$ ), while the energy exchanges in the form of heat are negligible. The precise position, line shape, and intensity of infrared absorption bands depend on the molecular structure and conformation as well as intra- and intermolecular interactions.<sup>8</sup> FTIR spectromicroscopy is therefore an imaging technique that is intrinsically label-free and requires minimal sample preparation. It also causes no detectable sample damage since the energy level of the infrared photons is not strong enough to break chemical bonds.<sup>9</sup> Thus, FTIR spectroscopy, together with bright field microscopy and Raman spectroscopy, is among the least invasive optical techniques available.

In recent years, FTIR spectromicroscopy witnessed major important advancements,<sup>10–12</sup> particularly the development of bright sources like synchrotrons<sup>13,14</sup> and tunable quantum cascade lasers.<sup>15,16</sup> Importantly, advances in detector technologies such as Focal Plane Arrays (FPA)<sup>17,18</sup> have enhanced the spatial resolution up to and beyond the diffraction limit ( $\leq 1 \mu\text{m}$  in the mid-IR range, 400–4000  $\text{cm}^{-1}$ ).

The main technical constraint in using infrared techniques to measure living biological samples is the overwhelmingly strong water signal.<sup>19,20</sup> For years a common approach was to only use FTIR to analyze dry or fixed biological samples, thereby completely removing the water absorption signal and its interference with the sample spectrum. However, this approach precludes the possibility to study live

<sup>a</sup> Berkeley Synchrotron Infrared Structural Biology Program, Lawrence Berkeley National Laboratory, 1 Cyclotron road, 94720 Berkeley, USA

<sup>b</sup> Elettra – Sincrotrone Trieste, Strada Statale 14 - km 163, 5 in AREA Science Park, 34149 Basovizza, Trieste, Italy

<sup>c</sup> Mechanobiology Institute (MBI), National University of Singapore, 5A Engineering Drive 1, 117411 Singapore, Singapore. E-mail: mbigg@nus.edu.sg

† Electronic supplementary information (ESI) available. See DOI: 10.1039/c5lc01460c

samples, such as cells maintained in culture media. To overcome this obstacle, several groups introduced microfluidic devices<sup>21–27</sup> or confined liquid compartments<sup>28</sup> which has enabled investigation of cellular processes such as cellular death,<sup>29</sup> cell cycle progression,<sup>30</sup> stem cell differentiation<sup>31</sup> or protein misfolding<sup>32</sup> at the single cell level and even with a subcellular spatial resolution.<sup>33</sup> However, the strategies adopted so far are often hampered by slow and expensive fabrication processes<sup>26,34</sup> leading to limited experimental flexibility.<sup>35</sup>

Here we present a new type of IR compatible microfluidic device, the IR-Live chip, which aims to reduce the cost and minimize the need to access an advanced microfabrication facility. With the exception of the initial standard lithographic step that is required to produce a reusable mould, the subsequent fabrication of a completely sealed closed-channel plastic microfluidic device featuring UV-VIS-IR transparent view-ports can be conducted in any laboratory equipped with an UV source. This new class of IR-compatible microfluidic device couples the benefits of using biocompatible polymers for the device's main body (e.g. easy connectivity to external systems, cheap and fast production, upscalability) with high optical performance within the view-port. To demonstrate the capability of IR-Live, we used an established rat embryo fibroblast cell line (REF52) as a model system. We first confirmed the ability of IR-Live to maintain cells in culture over 60 hours. Then we demonstrated the potential of IR-Live to minimize water-absorption interference while recording high-quality infrared spectra of the cells. We collected high spatial resolution chemical maps of migrating REF52 fibroblasts and analyzed them at the cellular and subcellular scales. Following this, we imaged U937 monocytes (a human leukemic monocyte lymphoma cell line) at three consecutive time points during their adaptation to the IR-Live chamber.

## Materials and methods

### IR-Live device fabrication

The detailed method of the device fabrication is described in the “Results” section. Briefly, a silicon master mould was prepared by UV lithography and silicon dry etching in an inductively coupled plasma (ICP) etching tool (SPTS Technologies Ltd., Ringland Way, Newport, NP18 2TA, UK). Then the master mould was replicated to generate a working one made from polydimethylsiloxane (PDMS) (184 Sylgard, Dow Corning MIDLAND, MI 48686-0994, USA). For the main body of the IR-Live, we used the optically clear liquid adhesive NOA 73 (Norland Adhesives, 2540 Route 130, Suite 100 Cranbury, NJ 08512, USA) as the UV-curable resin and IR-grade CaF<sub>2</sub> crystals were used for the view-ports (Crystran Ltd, 1 Broom Road Business Park Poole, Dorset, BH12 4PA, UK). The device was connected to the external pumps *via* metallic pins from New England Small tubes (Litchfield Technology Park, 480 Charles Bancroft Hwy., Litchfield, NH 03052, USA) and Eppendorf plastic tubes (Eppendorf AG, Barkhausenweg 1 22339 Hamburg, Germany).

The flow in the device was provided by a NE 1000 syringe pump (New Era Pump Systems, Inc., 138 Toledo Street Farmingdale, NY 11735-6625, USA).

### Cell culture and sample preparation

For the first set of experiments, adherent fibroblast REF52 cells were cultured in a 37 °C humidified incubator with 5% CO<sub>2</sub> on cell culture Petri dishes with Dulbecco's Modified Eagle Medium (DMEM) supplemented with 10% fetal calf serum (FCS). Passage of the attached cells was performed every 2 to 3 days by ethylenediaminetetraacetic acid (EDTA)/trypsin method. For infrared experiments, cells were detached from the Petri dish by the EDTA/trypsin method. Cells were then pelleted by centrifugation (1000 rpm for 3 min) to remove cell debris and trypsin, and then re-suspended in 1 mL of fresh DMEM medium with FCS. 100 µL of the cell suspension (~500 000 cells per mL) was transferred to the IR-Live device's reservoir. Using a syringe, negative pressure was applied from the outlet to the device to draw cells into the chamber. For the second set of experiments, the monocyte cell line U937 (American Type Culture Collection, Rockville, Md, USA<sup>36</sup>) was cultured in RPMI 1640 medium supplemented with 10% Fetal Bovine Serum (FBS), 2 mM L-glutamine and penicillin–streptomycin (100 U mL<sup>-1</sup>). Cells were maintained in an incubator at 37 °C with 5% CO<sub>2</sub> and cell passage was routinely done every three days. Before the experiment, cells were harvested, centrifuged at 500 rpm and suspended in fresh RPMI medium at a concentration of 1 × 10<sup>6</sup> cells per mL. U937 cells were then transferred into the fluidic IR-Live device as described above.

### Viability tests

Cell viability was accessed by means of a calcein retention/ethidium homodimer-1 exclusion assay (LIVE/DEAD Viability/Cytotoxicity Kit, Thermo Fisher Scientific). For comparison, REF52 cells were cultured for 24 h either on a CaF<sub>2</sub> crystal inside a standard Petri dish with 5 mL of growth medium placed inside an incubator (37 °C, 5% CO<sub>2</sub>), or cultured inside an enclosed IR-Live device under static conditions, or cultured inside an enclosed IR-Live device connected to a perfused system using a IM-Q BioStation (Nikon Corporation, Japan). Then, cells were treated with calcein (2 µM) and ethidium homodimer-1 (5 µM). After an additional 30-min incubation with calcein and ethidium homodimer-1, the medium was replaced by the HEPES-buffered saline solution. Images were acquired using an Olympus IX71 microscope equipped with a 4× objective.

### FTIR spectral imaging and analysis

Infrared experiments were carried out at the Berkeley Synchrotron Infrared Structural Biology (BSISB) program facility at the Advanced Light Source (ALS) beamline 5.4. Infrared images were acquired using a Hyperion 3000 IR VIS microscope equipped with a high power mid-IR source (W546/8 V glowbar) and a 128 × 128 photovoltaic MCT Focal Plane Array

(FPA) detector, which were coupled to a Vertex70V interferometer (Bruker Optik GmbH – Ettlingen, Germany). For the first experiment, which was designed to demonstrate the ability of the IR-Live to acquire chemical maps of REF52 cells with micrometer spatial resolution, we selected a  $36\times$  Schwarzschild objective/condenser pair (0.5 N.A.), resulting in a pixel size (and spatial resolution) of  $1.1 \times 1.1 \mu\text{m}^2$ . For the second experiment, which was designed to demonstrate the potential application of the IR-Live to measure the dynamics of biochemical processes in U937 cells, we used a  $15 \times 0.5$  N.A. objective granting a pixel size of  $2.5 \times 2.5 \mu\text{m}^2$ . Infrared spectral images were acquired by co-adding 512 scans per frame for REF52, and 256 scans per frame for the U937 cells with a  $4 \text{ cm}^{-1}$  spectral resolution, for a total acquisition time of 20 minutes or a temporal resolution of 10 minutes, respectively. Images of an empty chamber were acquired as background. Image analysis was done using OPUS 7.2 software (Bruker Optik GmbH – Ettlingen, Germany), which provided a standard pre-processing procedure to remove atmospheric water vapor and to make baseline correction *via* a rubber band algorithm with 5 iterations. Spectral contributions from aqueous culture media were removed by subtraction using a scaling factor proportional to the combination band (the bending vibration plus libration) of water (centered at  $2150 \text{ cm}^{-1}$ ).<sup>19,20</sup> Chemical maps were processed using R software and the hyperSpec package,<sup>37</sup> converted to a specified output using ENVI to generate baseline corrected data. Further image processing and analysis were performed using ImageJ. Data were analyzed further using Excel (Microsoft Office) and Prism (GraphPad). Chemical images of proteins (Amide II  $1480\text{--}1600 \text{ cm}^{-1}$ ), lipids ( $2800\text{--}3000 \text{ cm}^{-1}$ ), DNA (asymmetric stretching of phosphate band  $1190\text{--}1260 \text{ cm}^{-1}$ ) and RNA ( $1100\text{--}1160 \text{ cm}^{-1}$ , component of the symmetric stretching of the phosphate band) were obtained by integrating the respective peak area inside spectral regions, and shown as false color maps. Principal component analysis (PCA) was used to evaluate the chemical changes experienced within the cells after a 24 h period inside the device; the analysis was carried out using R and the spectral regions of interest were the lipid region ( $2800\text{--}3000 \text{ cm}^{-1}$ ) and the one for the proteins ( $1480\text{--}1700 \text{ cm}^{-1}$ ).

## Results and discussion

### IR-Live device – fabrication and characterization

Fig. 1 depicts the fabrication procedure. The PDMS working mould (Fig. 1A) was prepared as a cast replica of a silicon primary master mould *via* a standard photolithography methodology. We used a dry-etched silicon primary master mould with the purpose of increasing its lifetime. Nonetheless, for ease of fabrication, a perfectly equivalent primary master mould can be prepared in a single step through UV lithography, as shown in the ESI† (Fig. 1).

The PDMS replica mould features the microfluidic circuit in the form of a  $10 \mu\text{m}$  high protrusion; we used a very sim-

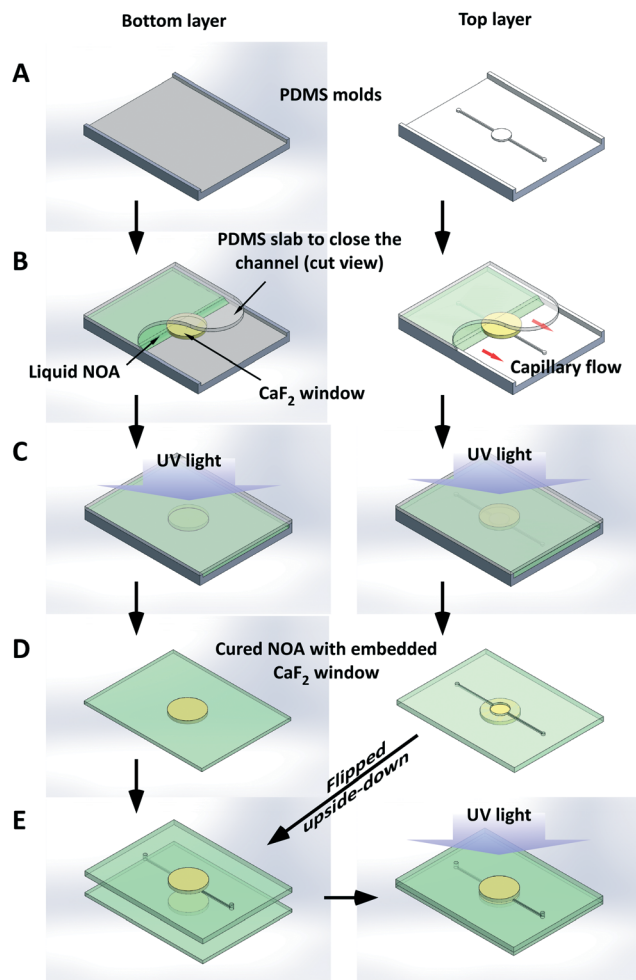


Fig. 1 Schematic of the proposed fabrication procedure. A) PDMS moulds are prepared for the bottom and top layers; the bottom layer (left) is a simple flat slab while the top one (right) carries the fluidic structures as protrusions  $10 \mu\text{m}$  thick. Each mould features a frame  $1 \text{ mm}$  thick to define the final size and shape of the device. B)  $\text{CaF}_2$  windows are placed in contact with the moulds and a flat PDMS cut is added to close the channel, which is filled with liquid NOA by capillarity. C) After complete filling, NOA is UV-cured. D) The solidified NOA is peeled off from its PDMS mould; on the structured half, holes are drilled corresponding to the inlet and outlet of the fluidic lay-out. E) The two NOA halves are brought in contact, gently pressed and further exposed to UV light to improve adhesion.

ple lay-out as a proof-of-principle, with a  $5 \text{ mm}$  wide circular central chamber accessed by an inlet channel ( $300 \mu\text{m}$  wide) and a similar outlet channel.

A  $\text{CaF}_2$  window ( $10 \text{ mm}$  diameter and  $1 \text{ mm}$  thick) was sandwiched between the mould and a flat cut of PDMS (Fig. 1A and B). About  $0.5 \text{ mL}$  of liquid NOA polymer was deposited on a short side of the sandwich and allowed to infiltrate by capillarity (Fig. 1B). The assembly was exposed to UV light for  $30 \text{ s}$  (Hg arc lamp, with an average intensity of  $10 \text{ mJ cm}^{-2}$  at  $365 \text{ nm}$ ) to partially cure the NOA. After peeling off from the PDMS master, holes aligned with the ends of the microfluidic channels were punched (ESI† Fig. S2). The resulting slab will serve as the top part of the final device.

Using the same procedure, a second  $\text{CaF}_2$  window was embedded in a flat NOA slab to produce the unstructured bottom half (Fig. 1C). Finally the two halves were pressed together and further exposed for 10 min, in order to terminate the curing of NOA and bond the device (Fig. 1D). The connection to the inlet of the pumping system was produced by inserting and gluing (with more NOA) of a metallic pin into one of the openings. On the outlet, a plastic reservoir was mounted to serve as a waste collector (see Fig. 2A). After sealing with more glue, the device was checked for leaks with a fluorescent probe. This involved filling the IR-Live device with a dilute solution of fluorescein ( $0.01 \text{ mg mL}^{-1}$ ), and imaging the device at  $4\times$  magnification with an Olympus IX71 microscope (Fig. 2B). Furthermore, IR spectral imaging of the spatial distribution of water absorption intensity was used to confirm the achievement of a good seal (ESI† Fig. 3). IR maps also demonstrate the absence of any interference arising from the polymer.

### Cell viability within the IR-Live device

All materials used in the construction of the IR-Live chip are known to be biocompatible.<sup>38,39</sup> However, there was a concern whether the required  $10\text{-}\mu\text{m}$  height would introduce sufficient mechanical stress to affect the cells' viability or other behavior.

To address the first concern of viability, we first cultured REF52 cells under three different conditions: on an open  $\text{CaF}_2$  window embedded in a NOA73 slab (ESI† Fig. S4); in an IR-Live device and cultured at  $37^\circ\text{C}$  without medium exchange for 24 h, or in an IR-Live device with a continuous medium exchange at a flow rate of  $8 \mu\text{L h}^{-1}$  for  $>60 \text{ h}$  at  $37^\circ\text{C}$ ,  $5\% \text{ CO}_2$ . Results from the calcein retention/ethidium homodimer-1 exclusion assay showed that a large majority of cells ( $99.68\% \pm 0.44$ ) appeared to be alive under the first culture conditions (Fig. 3A).

Next, we assessed the morphology and behavior of cells injected into the fully sealed IR-Live device by observing them under a Nikon IM-Q Biostation, a microscope equipped with an environmental chamber which maintains optimal cultur-

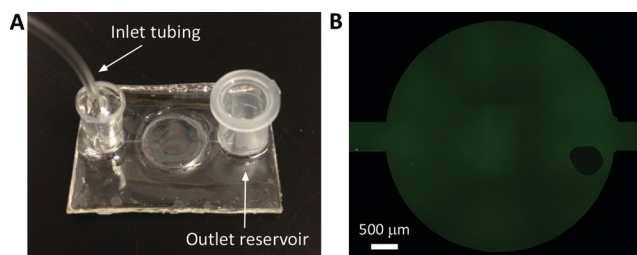


**Fig. 2** A) The IR-Live device with a white inlet tubing and outlet attached to the reservoir. In the centre of the device is the IR-transparent experimental chamber sandwiched between two  $\text{CaF}_2$  crystal discs. B) A mosaic image of the central chamber of the IR-Live device, which was filled with a fluorescein solution ( $0.01 \text{ mg mL}^{-1}$ ). The black spot in the chamber is a small air bubble trapped in the device for the purpose of contrasting illustration.

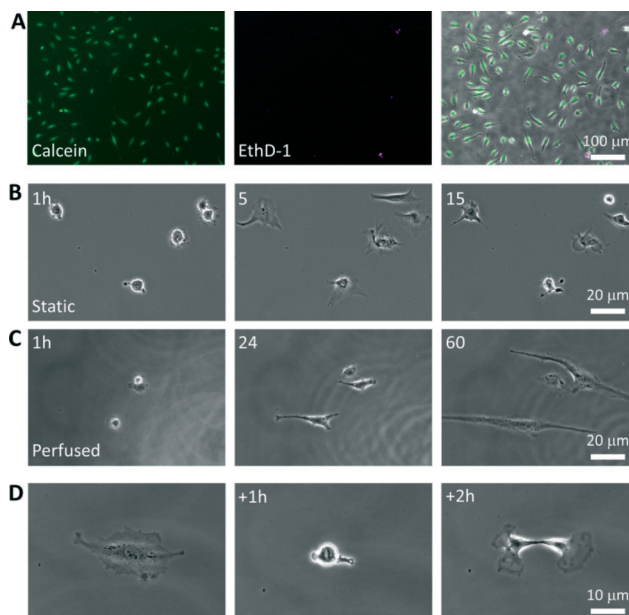


**Fig. 3** Results of viability tests. A) REF52 cells cultured on a  $\text{CaF}_2$  substrate embedded in NOA73 are stained with calcein (green) and ethidium homodimer-1 (red). Retention of calcein indicates the presence of live, metabolically-active cells. Red staining of the nucleus occurs only in dead cells where the cell membrane is damaged. B) Cells grown in a closed IR-Live device under static conditions (*i.e.* without exchange of medium). The small, confined environment allows cells to survive only for less than 15 h. After that time, near synchronous apoptosis occurred for all cells under observation. C) Cells grown under perfused conditions (*i.e.* subject to continuous flow of fresh medium) survived for the entire period of observation ( $>60 \text{ h}$ ). D) Under perfused conditions, cells were able to perform physiological functions such as mitosis and cell migration.

ing conditions ( $37^\circ\text{C}$  and  $5\% \text{ CO}_2$ ). Tests were performed under static conditions (*i.e.* without exchange of medium) and perfusion (flow rate =  $8 \mu\text{L hr}^{-1}$ , allowing 100% medium exchange in the recording chamber every minute). For both conditions, the IR-Live device filled with medium was placed inside the environmental chamber for 2 hours to allow equilibration of temperature and  $\text{CO}_2$  before introducing the microliter cell suspension (ESI† Fig. S5). Under static conditions (Fig. 3B), cells spread and attached to the  $\text{CaF}_2$  surface within an hour. After 5 hours, the cells exhibited a polarized morphology and started migrating. However, after 14 hours, cell death occurred due to a lack of nutrients and presumably an accumulation of metabolic by-products (ESI† movie 1). Under perfusion conditions, a  $\text{CO}_2$ -permeable silicone tubing was used to connect an external syringe pump (New Era 1000NE) to the inlet of the IR-Live device since both NOA73 and  $\text{CaF}_2$  are not permeable to gases. A total of 1 meter of silicone tubing was coiled inside the environmental chamber. After a 2-hour equilibration time, we drew in suspended cells from the outlet reservoir inside the environmental chamber into the central observation chamber. Under these conditions (Fig. 3C), cells proved to be viable and motile and we never observed apoptotic events during the time of observation ( $>60 \text{ h}$  – ESI† movie 2). Furthermore, we witnessed a few

mitosis events (Fig. 3D and ESI† movie 3), implying that cells are cultured under optimal conditions.

### High-resolution spatially resolved chemical maps of migrating REF52 fibroblasts

We first demonstrated the potential utility of IR-Live as a high spatial resolution FTIR chemical imaging technique. 1  $\mu\text{L}$  of a REF52 cell suspension (approx. 500 to 1000 cells) was pipetted into the outlet chamber of the IR-Live device. Using a 1 mL syringe connected to the inlet tubing, cells were pulled and transferred inside the  $\text{CaF}_2$  chamber. Thereafter, the IR-Live device was kept inside the cell culture incubator for 2 hours to allow the cells to adapt to the new conditions, and to adhere and spread onto the substrate surface. After two hours, the IR-Live device was flushed with the fresh medium to remove unattached cells and mounted on the temperature-controlled microscope stage at the IR beamline (Fig. 4A). Several groups of cells were visually selected according to their shape and morphology for subsequent IR spectral imaging. We subsequently employed a 36x Schwarzschild objective/condenser pair (0.5 N.A.), which yields a pixel size of  $1.2 \times 1.2 \mu\text{m}^2$ . For each pixel within a

field of view of  $\sim 69 \mu\text{m}$  by  $69 \mu\text{m}$ , a corresponding full spectrum of chemical absorption between  $4000$  and  $900 \text{ cm}^{-1}$  was acquired (Fig. 4C). By integrating the absorption peaks in the  $\text{CH}_2\text{-CH}_3$  stretching ( $3000\text{--}2800 \text{ cm}^{-1}$ ) region, we obtained the spatial distribution of lipid molecules (Fig. 4B). Likewise, integration of the signal in the amide II absorption envelope in the  $1600\text{--}1480 \text{ cm}^{-1}$  region was used to map the spatial distribution of proteins.

Analysis of the spatially resolved distribution of proteins and lipids revealed that the REF52 cells displayed characteristic shapes of motile cells (ESI† Fig. S6A) with a pronounced rear–front polarity (compared to the direction of motion). From all the spectral heat maps analyzed (Fig. 4B), we identified a cell with a typical spindle shape; its morphology and rear–front polarity could be easily identified (see ESI† Fig. S6B). Interestingly, the chemical maps of this cell indicated a strong rear–front as well as left–right asymmetry of lipid and protein distributions (Fig. 5A). In particular, the line plot starting from the rear of the cell (Fig. 5B, Line 1, arrow head a) showed that both chemical species increased in abundance, an observation which is compatible with the transition between the retracting flat regions at the trailing end of the cell to the cell body. While protein absorbance increased steadily and reached a peak at  $x = 45 \mu\text{m}$  (Fig. 5B, Line 1, arrow head c), lipids showed a transient plateau (Fig. 5B, Line 1, arrow head b). This might reflect the presence of the nucleus in this region, which is mostly composed of the nucleic acids and histone proteins enclosed within a single phospholipid bilayer. The spectral map also showed a lipid and protein rich compartment ahead of this region (Fig. 5A). In most migrating cells, they translocate forward to the nucleus, a large portion of the endoplasmic reticulum, the Golgi apparatus and secretory vesicles, to readily provide the migratory machinery with freshly synthesized proteins and membrane lipids. Away from this chemically rich region (Fig. 5B, Line 1, arrow head d), both lipid and protein signals sharply declined with distance until reaching a region where the protein absorbance remained dominant while the lipid absorbance nearly vanished. This would be consistent with the presence of the lamellipodium at the front of a migrating cell. This migratory structure is composed mostly of actin-binding proteins and cross-linked actin filaments that are closely associated with the cell membrane. Interestingly, this protein rich structure extended from the front to the left side of the cells (Fig. 5B, Line 2, arrow head f). A finer analysis of the chemical composition of this structure revealed the following information. Point “b”, identified as belonging to the nucleus, has a sharp protein signal centered at  $1654 \text{ cm}^{-1}$  which is mainly attributed to an  $\alpha$ -helix protein structure. At points “d” and “f”, located near the front of the cell, there was a  $2 \text{ cm}^{-1}$  red shift of two  $\text{CH}_2$  bands, from  $2925 \text{ cm}^{-1}$  and  $2853 \text{ cm}^{-1}$ , to  $2923 \text{ cm}^{-1}$  and  $2851 \text{ cm}^{-1}$ , respectively. This suggests a higher lipid organization at this pole of the cell. The data suggest that there is a compartmentalization of the plasma membrane, which at the front seems to contain more ordered lipid domains than the other regions of the cell.

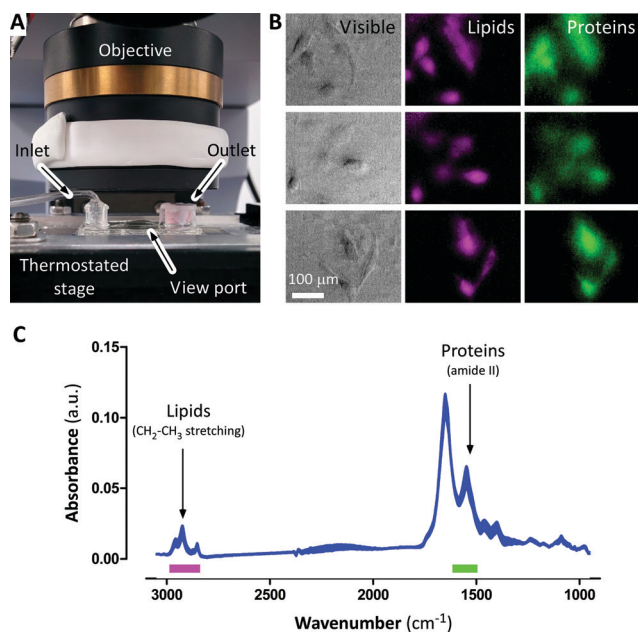


**Fig. 4** A) A close-up photo of the experimental setup at the BSISB infrared beamline 5.4.1 at the ALS. The IR-Live device was placed on a heating stage set at  $37 \text{ }^\circ\text{C}$  under a 36x objective lens of a Hyperion 3000 IR/VIS microscope. B) Several groups of motile REF52 cells. Transmitted visible light micrographs (bright field) and spatially resolved chemical spectral heat maps of proteins (magenta) and lipids (green) are shown. The Schwarzschild objectives of medium/high magnification factor do not yield good optical contrast in the visible spectral range, therefore the quality of the bright field images generally did not contrast well and details of the migrating cell such as cellular organelles and protrusions are blurred. C) Absorption spectra of the measured cells, presented as an average spectrum  $\pm$  standard deviation ( $n = 14$  cells). Color bars represent spectral regions used to quantify lipids (magenta) and proteins (green).

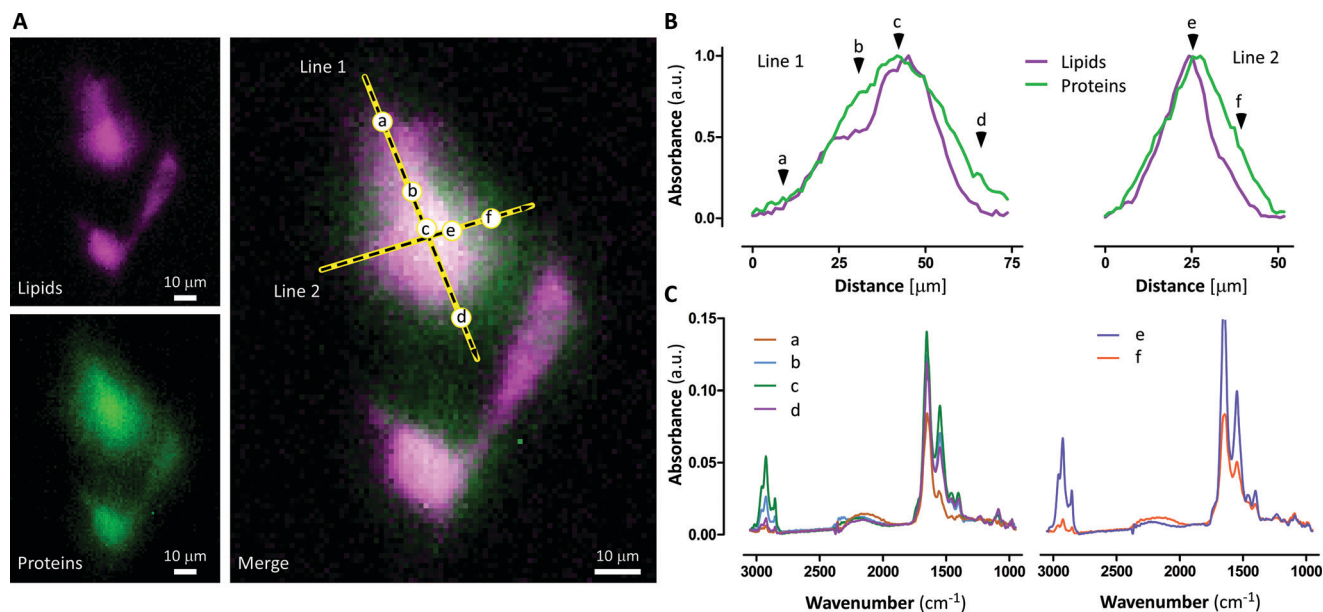


**Fig. 5** A) Images of high-resolution spatially resolved chemical maps of protein (magenta) and lipids (green) are shown in the left panels, and merged (right panel). B) Line profiles of the integrated infrared absorbance lipids (purple) and proteins (green). The 75- $\mu\text{m}$  long Line 1 starts at the trailing rear of the cell and ends at the front. Line 2 spans from the right side of the cells to the left side relative to the direction of movement. To reduce random noise, the line image is an average of 4 pixels (about 4.4  $\mu\text{m}$  wide). C) Adsorption spectra at different areas (4  $\times$  4 pixels, about 20  $\mu\text{m}^2$ ) within the cell.

To highlight the main spectral features that change after 24 h inside the device, we performed a PCA analysis on the data collected at  $t_0 = 0$  and  $t_1 = 24$  h, (see ESI† Fig. S7). Principal component 1 mainly describes variations on the protein content, whereas principal component 2 is related more to modifications of the lipids. From this analysis we cannot observe a trend in the variation of proteins, as it was expected since the cells were not synchronized. An increase in the lipid content is clear, and it can be related to the spreading of the membrane onto the surface, typical of this cell line that is known for its high motility.

#### Time-resolved chemical maps of U937 monocytes during adaptation

We also demonstrated the potential utility of the IR-Live as a real-time chemical imaging tool by performing a simple experiment imaging the transient spectral signatures of cells within the first hour of their adaptation to the IR-Live chamber after the injection. For this experiment, we used U937 monocytes. These cells are easy to inject into the device as they are quite small ( $\sim 10$   $\mu\text{m}$  in diameter). We chose a 15 $\times$  objective (*i.e.* a pixel size of  $2.62 \times 2.62$   $\mu\text{m}^2$ ), which was about two-fold coarser in spatial resolution than that of the experiment with REF52 cells. However, the benefits of this lower magnification are as follows: a larger field of view; higher signal-to-noise ratio; lesser number of scans required, thus enabling a more detailed temporal resolution. Time-course analysis of the FTIR image measurements starting with the introduction of cells into the IR-Live chamber shows a sequence of biomolecule synthesis events during the adaption of the cells to the bio-compatible

surface, or the so called “settling down phase”, as shown in Fig. 6A–D. In the comparison of the U937 spectra in Fig. 6C with those in Fig. 4C from REF52 fibroblasts, we can see some differences in the relative composition of lipids and proteins. This clearly indicates that every cell type has a slightly different IR spectrum, which is important as it demonstrates that FTIR using IR-Live provides sufficient details for cell recognition. Initially, the U937 cells could have been at a resting state because of the handling process required before injection. During the first 30 minutes, we observed a  $\sim 14\%$  increase in the intensity of the phosphodiester  $\nu_{\text{as}}(\text{PO}_2^-)$  groups of phosphorylated proteins or DNA/RNA polysaccharide backbone structure ( $\sim 1233$   $\text{cm}^{-1}$ ) and a  $\sim 5\%$  increase in the signal of protein amide II. An increase in the absorption intensity in the 966–930  $\text{cm}^{-1}$  area together with an increase at  $\sim 1082$  and  $\sim 1233$   $\text{cm}^{-1}$  could be attributed to protein phosphorylation.<sup>24</sup> In the following 30 minutes, the infrared absorption intensity of protein amide II and of the lipid signals increased by  $\sim 20\%$ . In contrast, the signals from the  $\nu_{\text{as}}(\text{PO}_2^-)$  groups of phosphorylated proteins reached a plateau, or even decreased slightly. This transient behavior of the infrared signals of protein phosphorylation is consistent with those reported earlier.<sup>25</sup>

## Summary & conclusions

We have demonstrated a protocol to build a low-cost IR-Live microfluidic chip for real-time 2D infrared imaging of living cells or tissues with a spatiotemporal resolution in the range of micrometers and minutes. In previously published work,<sup>21,40–42</sup> FTIR compatible microfluidic chips were produced by direct photolithography of a resist layer coated onto

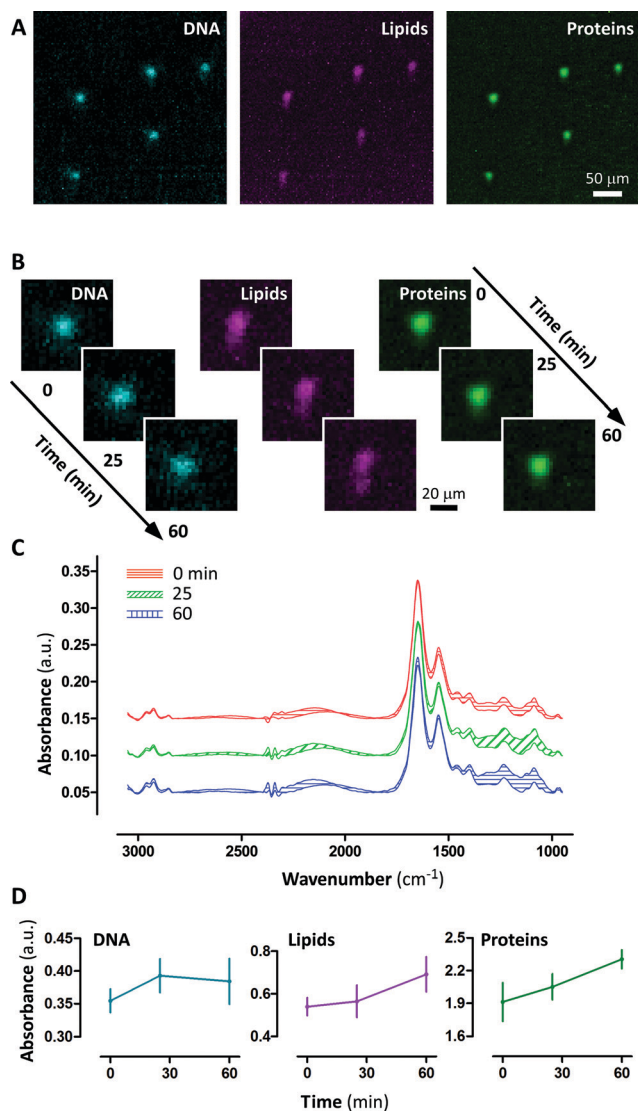


**Fig. 6** Spatial and temporal distributions of DNA, lipids and proteins. A) FTIR chemical maps of U937 monocytes, showing the spatial distribution of the main cellular components (DNA, lipids and proteins, respectively). The acquisition time for each frame was 10 minutes. B) Time-dependent evolution of the average spectra of U937 monocytes. C) An example of time-dependent changes in the cellular chemistry as expressed by the absorption spectra at different time points; each time point is expressed by an average spectrum ( $n = 5$  cells)  $\pm$  standard deviation. D) Plots of the time variation of the integrated average absorption peak intensity for protein phosphorylation, lipids, and protein contents.

one large IR window (40 mm diameter). Although suitable for FTIR experiments, that approach suffered from two major drawbacks: the use of a large IR window as the whole substrate, in which holes for fluidic connections have to be directly drilled in, and the need of a photolithographic step to be performed for each single device. We argue that these limitations could reduce the general applicability of that approach to a broader community of FTIR users. Here we used a very simple microfluidic layout to demonstrate a new fabrication scheme aimed at solving these issues.

Using a plastic frame as the main body of the final IR-Live device will enable designing and building more complex microfluidic layouts for infrared imaging of living samples in real-time, since it removes the need for micromachining the IR/VIS transparent window. Most importantly, it confines the requirement of a 10- $\mu\text{m}$  thick medium layer to the view-port area only. Furthermore, the fabrication approach proposed here reduces the need to access a microfabrication laboratory only for the production of a primary master mould; all the subsequent steps can be carried out in any lab equipped for standard soft lithography. We demonstrated that cells do not suffer in the 10- $\mu\text{m}$  spatial confinement even for experiments lasting multiple days. Cells are able to attach and proliferate inside the IR-Live device if nutrients are provided and wastes are removed.

From our results of IR imaging on migrating cells with sub cellular spatial resolution, we were able to distinguish different cellular organelles and identify their peculiar chemical composition at a functional group level. We also presented results from using the IR-Live chip to unravel the behavior of cells as they were adapting to the IR-Live device. Temporal and spatial resolutions of this IR-mapping configuration can be adjusted according to a range of experimental parameters such as cell type, cell size, or signal-to-noise ratio. This novel approach will offer great, perhaps even revolutionary, new capabilities for the future of infrared imaging of living biosystems in biological, microbial, or biomedical research.

## Acknowledgements

We acknowledge financial support from the Mechanobiology Institute (MBI), National University of Singapore, through an internal seed grant.

This work was performed in part under the Berkeley Synchrotron Infrared Structural Biology (BSISB) Program funded by the US Department of Energy, Office of Science, and Office of Biological and Environmental Research. The Advanced Light Source is supported by the Director, Office of Science, and Office of Basic Energy Sciences. Both were supported through Contract DE-AC02-225 05CH11231.

The authors acknowledge A. Wong and J. Shanmugarajah of the Mechanobiology Institute for help in editing the manuscript.

## Notes and references

- 1 B. Neumann, T. Walter, J. K. Heriche, J. Bulkescher, H. Erfle, C. Conrad, P. Rogers, I. Poser, M. Held, U. Liebel, C. Cetin, F. Sieckmann, G. Pau, R. Kabbe, A. Wunsche, V. Satagopam, M. H. Schmitz, C. Chapuis, D. W. Gerlich, R. Schneider, R. Eils, W. Huber, J. M. Peters, A. A. Hyman, R. Durbin, R. Pepperkok and J. Ellenberg, *Nature*, 2010, **464**, 721–727.
- 2 W. Choi, C. Fang-Yen, K. Badizadegan, S. Oh, N. Lue, R. R. Dasari and M. S. Feld, *Nat. Methods*, 2007, **4**, 717–719.
- 3 S. W. Hell and J. Wichmann, *Opt. Lett.*, 1994, **19**, 780–782.

- 4 T. D. Lacoste, X. Michalet, F. Pinaud, D. S. Chemla, A. P. Alivisatos and S. Weiss, *Proc. Natl. Acad. Sci. U. S. A.*, 2000, **97**, 9461–9466.
- 5 L. Schermelleh, P. M. Carlton, S. Haase, L. Shao, L. Winoto, P. Kner, B. Burke, M. C. Cardoso, D. A. Agard, M. G. Gustafsson, H. Leonhardt and J. W. Sedat, *Science*, 2008, **320**, 1332–1336.
- 6 M. F. Juette, T. J. Gould, M. D. Lessard, M. J. Mlodzianowski, B. S. Nagpure, B. T. Bennett, S. T. Hess and J. Bewersdorf, *Nat. Methods*, 2008, **5**, 527–529.
- 7 S. R. Pavani, M. A. Thompson, J. S. Biteen, S. J. Lord, N. Liu, R. J. Twieg, R. Piestun and W. E. Moerner, *Proc. Natl. Acad. Sci. U. S. A.*, 2009, **106**, 2995–2999.
- 8 H. H. Mantsch and D. Chapman, *Infrared spectroscopy of biomolecules*, Wiley-Liss, New York, 1996.
- 9 H. Y. Holman, K. A. Bjornstad, M. P. McNamara, M. C. Martin, W. R. McKinney and E. A. Blakely, *J. Biomed. Opt.*, 2002, **7**, 417–424.
- 10 P. Dumas, G. L. Carr and G. P. Williams, *Analyst*, 2000, **28**, 68–74.
- 11 L. M. Miller and P. Dumas, *Bba-Biomembranes*, 2006, **1758**, 846–857.
- 12 G. L. Carr, *Rev. Sci. Instrum.*, 2001, **72**, 1613–1619.
- 13 M. J. Nasse, M. J. Walsh, E. C. Mattson, R. Reininger, A. Kajdacsy-Balla, V. Macias, R. Bhargava and C. J. Hirschmugl, *Nat. Methods*, 2011, **8**, 413–U458.
- 14 E. Stavitski, R. J. Smith, M. W. Bourassa, A. S. Acerbo, G. L. Carr and L. M. Miller, *Anal. Chem.*, 2013, **85**, 3599–3605.
- 15 K. Yeh, S. Kenkel, J. N. Liu and R. Bhargava, *Anal. Chem.*, 2015, **87**, 485–493.
- 16 N. Kroger-Lui, N. Gretz, K. Haase, B. Kranzlin, S. Neudecker, A. Pucci, A. Regenscheit, A. Schonhals and W. Petrich, *Analyst*, 2015, **140**, 2086–2092.
- 17 E. N. Lewis, P. J. Treado, R. C. Reeder, G. M. Story, A. E. Dowrey, C. Marcott and I. W. Levin, *Anal. Chem.*, 1995, **67**, 3377–3381.
- 18 R. Blanchard, S. V. Boriskina, P. Genevet, M. A. Kats, J. P. Tetienne, N. Yu, M. O. Scully, L. Dal Negro and F. Capasso, *Opt. Express*, 2011, **19**, 22113–22124.
- 19 K. Rahmelow and W. Hubner, *Appl. Spectrosc.*, 1997, **51**, 160–170.
- 20 S. Y. Venyaminov and F. G. Prendergast, *Anal. Biochem.*, 1997, **248**, 234–245.
- 21 E. Mitri, G. Birarda, L. Vaccari, S. Kenig, M. Tormen and G. Greci, *Lab Chip*, 2014, **14**, 210–218.
- 22 L. Vaccari, G. Birarda, G. Greci, S. Pacor and L. Businaro, *J. Phys.: Conf. Ser.*, 2012, 359.
- 23 E. J. Marcsisin, C. M. Uttero, M. Miljkovic and M. Diem, *Analyst*, 2010, **135**, 3227–3232.
- 24 L. Chen, H. Y. N. Holman, Z. Hao, H. A. Bechtel, M. C. Martin, C. B. Wu and S. Chu, *Anal. Chem.*, 2012, **84**, 4118–4125.
- 25 H. Y. N. Holman, H. A. Bechtel, Z. Hao and M. C. Martin, *Anal. Chem.*, 2010, **82**, 8757–8765.
- 26 B. Lehmkuhl, S. D. Noblitt, A. T. Krummel and C. S. Henry, *Lab Chip*, 2015, **15**, 4364–4368.
- 27 P. Heraud, B. R. Wood, M. J. Tobin, J. Beardall and D. McNaughton, *FEMS Microbiol. Lett.*, 2005, **249**, 219–225.
- 28 M. J. Nasse, S. Ratti, M. Giordano and C. J. Hirschmugl, *Appl. Spectrosc.*, 2009, **63**, 1181–1186.
- 29 G. Birarda, D. E. Bedolla, E. Mitri, S. Pacor, G. Greci and L. Vaccari, *Analyst*, 2014, **139**, 3097–3106.
- 30 D. E. Bedolla, S. Kenig, E. Mitri, P. Ferraris, A. Marcello, G. Greci and L. Vaccari, *Analyst*, 2013, **138**, 4015–4021.
- 31 C. Sandt, J. Frederick and P. Dumas, *J. Biophotonics*, 2013, **6**, 60–72.
- 32 G. Hoffner, W. Andre, C. Sandt and P. Djian, *Rev. Anal. Chem.*, 2014, **33**, 231–243.
- 33 L. M. Miller, M. W. Bourassa and R. J. Smith, FTIR spectroscopic imaging of protein aggregation in living cells, *Biochimica Et Biophysica Acta-Biomembranes*, 2013, **1828**(10), 2339–2346.
- 34 G. Greci, G. Birarda, E. Mitri, L. Businaro, S. Pacor, L. Vaccari and M. Tormen, *Microelectron. Eng.*, 2012, **98**, 698–702.
- 35 M. J. Tobin, L. Puskar, R. L. Barber, E. C. Harvey, P. Heraud, B. R. Wood, K. R. Bambery, C. T. Dillon and K. L. Munro, *Vib. Spectrosc.*, 2010, **53**, 34–38.
- 36 C. Sundstrom and K. Nilsson, *Int. J. Cancer*, 1976, **17**, 565–577.
- 37 C. Beleites and V. Sergo, *hyperSpec: a package to handle hyperspectral data sets in R*, 2011, Available from: <http://hyperspec.r-forge.r-project.org/>.
- 38 E. Sollier, C. Murray, P. Maoddi and D. Di Carlo, *Lab Chip*, 2011, **11**, 3752–3765.
- 39 K. Wehbe, J. Filik, M. D. Frogley and G. Cinque, *Anal. Bioanal. Chem.*, 2013, **405**, 1311–1324.
- 40 L. Vaccari, G. Birarda, L. Businaro, S. Pacor and G. Greci, *Anal. Chem.*, 2012, **84**, 4768–4775.
- 41 G. Birarda, G. Greci, L. Businaro, B. Marmiroli, S. Pacor and L. Vaccari, *Microelectron. Eng.*, 2010, **87**, 806–809.
- 42 G. Birarda, G. Greci, L. Businaro, B. Marmiroli, S. Pacor, F. Piccirilli and L. Vaccari, *Vib. Spectrosc.*, 2010, **53**, 6–11.